International Journal of Pure and Applied Mathematics
Volume 79 No. 3 2012, 425-452
ISSN: 1311-8080 (printed version)
url: http://www.ijpam.eu

MATHEMATICAL MODELING FOR HOLLOW FIBER DIALYZER: BLOOD AND HCO_3^--DIALYSATE FLOW CHARACTERISTICS

Kodwo Annan

Department of Mathematics and Computer Science
Minot State University
Minot, North Dakota, 58707, USA

Abstract: In an attempt to improve the quality and efficacy of Hemodialysis (HD) therapy, dialyzers headers have been redesigned to improve uniform blood and dialysate flows. Any mismatch caused by non-uniform flow distributions in either blood or dialysate compartment would result in inefficiency of a dialyzer. Mathematical modeling technique was used to investigate and provide insights into the flow distributions during dialysis session. A suite of convection-diffusion models for blood and dialysate counter-current flows were deployed. The model coupled blood and dialysate side geometries through a Trans-membrane layer using Kedem-Katchalsky equations. The blood flow distributions were observed to be uniform across each cross-section while a non-uniform dialysate flow distributions were observed near the hollow-fiber packing area at the dialysate-side. The uniform blood-side flow distribution suggested that the new blood header design used in modern hollow-fiber dialyzers was an efficient flow distributor. The non-uniform dialysate flow profile indicated that the collars used in existing hollow-fiber dialyzers to help dialysate uniform flow failed to promote uniform flow. Consequently, the flow distributions mismatch in the dialyzer affected the boundary and bulk solute concentrations exchange

Received: April 26, 2012

© 2012 Academic Publications, Ltd.
url: www.acadpubl.eu

across the membrane. The flow distribution analysis may have practical significances for the design of high efficient hollow-fiber dialyzers.

Key Words: mathematical modeling, hollow fiber, dialyzer, blood flow

1. Introduction

Hollow-fiber dialyzers are life-saving devices that extend life by removing toxins that accumulate in end-stage kidney disease patients. Small solutes are normally removed by diffusion while larger solutes are mostly removed by convection through ultra-filtration. Therefore, the efficiency of a hollow-fiber dialyzer depends on its ability to facilitate both diffusion and convection processes [1-2]. Diffusion in particular, is affected by blood and dialysate flow rates, dialyzer membrane thickness and surface area, and temperature. Assuming dialyzer surface area and temperature are kept constant, diffusion is strongly affected by blood and dialysate flow rates and flow distributions in their respective compartments. It is widely accepted that the flow distributions mismatch in the dialyzer creates a significant reduction in the efficiency of the dialyzer [3-4]. As a result of the inefficiency and the difficulty in the regulatory mechanisms, the quality of life for many End-Stage Renal Disease (ESRD) patients is still unsatisfactory [5]. Hypertension and other pathologies associated with ESRD patients receiving dialysis therapy remain high [6-11].

In recent years, research studies were deployed in the design of high efficient hollow-fiber dialyzers [12-18]. Majority of these research required analysis of blood, dialysate, and ultra-filtration (UF) flows inside the dialyzer with flow devices [14], [16-18]. However, an intrusion of tiny flow device into a hollow-fiber dialyzer is practically impossible due to high dense bundled fibers inside the dialyzer. A mathematical modeling approach of the hollow-fiber dialyzer that gives insight of blood and dialysate flow distributions is of paramount importance.

In addition, most clinical studies investigated flow distributions at the blood or the dialysate side of a hollow-fiber dialyzer [3, 14, 16-21]. For blood side investigation, flow rate measurements were taken at the intermediate, central, and peripheral cross sectional areas, respectively, of the hollow fiber bundle. High flow rate was recorded at the peripheral areas, followed by the intermediate and the central regions of the hollow fiber bundle. The non-uniform flow distributions were attributed to the inlet manifold used by the dialyzer's manufacturer [19-20]. X-ray computed tomography (CT) scanner and a radio-opaque tracer dye were used to examine the dialysate flow distribution in hollow fiber dialyzers

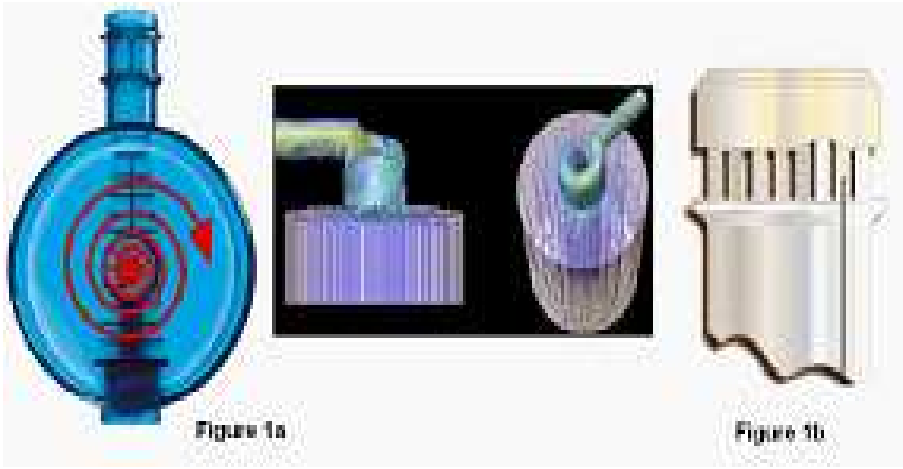

Figure 1: (a) Path lines of Blood flow inside the flange for FME Dialyzers. 1(b) Pinnacle Assembly and New Potting Technology at the ends of new hollow-fiber dialyzer headers to promote uniform dialysate flow distribution. (FME 2005)

[3]. Non-uniform dialysate flow distribution was recorded with the fastest and slowest flows rates occurring at the outer and the inner cross sectional regions, respectively.

In an attempt to resolve non-uniform flow distributions in dialyzers, new blood and dialysate headers have been introduced by dialysis manufacturers. In the Fresenius construct, for example, the blood enters through a lateral inlet port (Figure 1a) while the dialysate passes through a pinnacle structure (Figure 1b). Clinical investigations on new dialyzer header designs with magnetic resonance imaging (MRI) technology indicated relatively uniform blood flow and non-uniform dialysate flow distributions [21, 23-25].

Blood and/or dialysate flow investigations using mathematical modeling have been extensively discussed in many articles [26-33]. In most of the modeling techniques, uniform membrane flux, uniform blood flow, and constant dialysate concentration were assumed. These assumptions seem to be unrealistic. In fact, the dialysate concentration would not be constant and ions such as bicarbonate would be transported across the membrane during dialysis sessions [22] and [49]. In addition, modern dialyzers are modeled with high flux membranes causing high UF and back-filtration (BK) flow rates which results in non-uniform TM flux across the dialyzer membrane. Liao et al. [35] coupled shell- and lumen- sides with TM flow calculated by the Kedem-Katchalsky

(K-K) equations. However, their model did not examine the lumen side flow and more importantly did not include bicarbonate buffer mostly used to treat ESRD patients suffering from metabolic acidosis.

In this paper, flow characteristics of a typical bicarbonate based HD therapy were presented. A suite of convection-diffusion models for blood and dialysate counter-current flows were deployed. The model couples blood and dialysate geometries through a TM layer using K-K equations. The resulting model was numerically solved using Finite Volume Technique and MATLAB software tool. Numerical results showed that flow characteristics influence the distribution and exchange of small solutes concentrations such as bicarbonate and carbon dioxide during HD therapy.

The paper was organized as follows: Assumptions, model description, and numerical techniques were presented in the next two sections. Numerical results and discussions were presented afterwards. The paper ended with a summary.

2. Model Formulation

From a mathematical modeling perspective, typical hollow-fiber dialyzer geometry uses countercurrent blood and dialysate flows separated by hollow-fiber membrane (Figure 2a). Blood flows inside the hollow-fibers whereas dialysate flows outside the hollow-fiber region counter currently. In this geometry construct, a raised collar with a small plate distributor is placed near dialysate inlet and outlet to promote homogeneous distribution at the dialysate side. The plate distributor prevents dialysate fluid from entering the fiber bundle directly, thus causing the inlet fluid to impinge on the distributor, then going around the collar before penetrating into the fiber bundle. Similarly, the distributor facing the outlet causes outlet dialysate to first flow out from the fiber bundle and then around the collar before exiting.

2.1. Blood-Side Flow

Let (z, r) be the coordinates of the representative point in the cylindrical coordinate system where the z-axis is taken along the dialyzer length (i.e. $0 \leq z \leq L$) and r is taken along the radial direction. Considering an axisymmetric domain, r is chosen to lie in the range $0 < r < r_b$ between $z = 0$ *and* $z = L$ for a membrane length L and radiusr_b. The blood-side computational domain of the model is shown in Figure 2b.

The Navier-Stokes and continuity equations that govern the steady fully

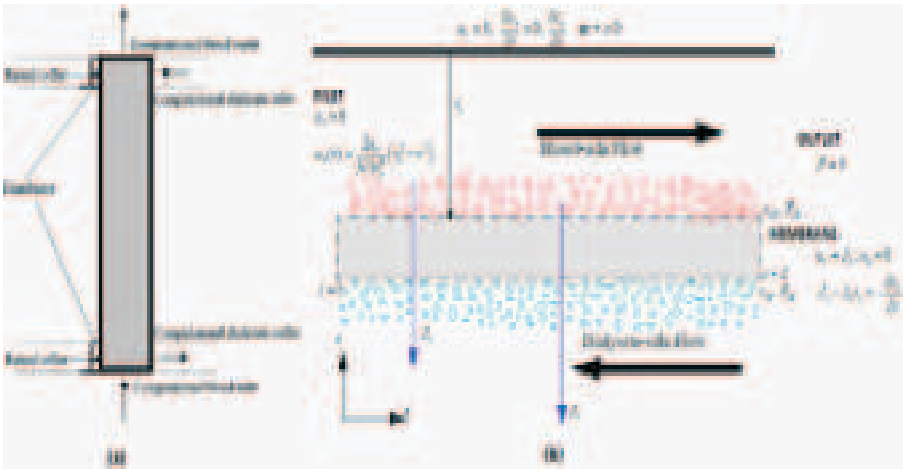

Figure 2: (a) Schematic of a typical hollow-fiber dialyzer module with the computational blood and dialysate domains. (b) Mass transport of solutes in blood and dialysate compartments through a single hollow fiber membrane.

developed flow of an incompressible Newtonian fluid representing blood with density ρ and viscosity μcan be described as [22] and [49]:

$$\begin{aligned}
&\tfrac{1}{r}\tfrac{\partial(ru_r)}{\partial r} + \tfrac{\partial u_z}{\partial z} = 0,\\
&u_r\tfrac{\partial u_r}{\partial r} + u_z\tfrac{\partial u_r}{\partial z} = -\tfrac{1}{\rho}\tfrac{\partial p}{\partial r} + \tfrac{\mu}{\rho}\left[\tfrac{1}{r}\tfrac{\partial}{\partial r}\left(r\tfrac{\partial u_r}{\partial r}\right) - \tfrac{u_r}{r^2} + \tfrac{\partial^2 u_r}{\partial z^2}\right],\\
&u_r\tfrac{\partial u_z}{\partial r} + u_z\tfrac{\partial u_z}{\partial z} = -\tfrac{1}{\rho}\tfrac{\partial p}{\partial z} + \tfrac{\mu}{\rho}\left[\tfrac{1}{r}\tfrac{\partial}{\partial r}\left(r\tfrac{\partial u_z}{\partial r}\right) + \tfrac{\partial^2 u_z}{\partial z^2}\right],
\end{aligned} \tag{1}$$

where u_r and u_z are the radial and axial velocity components, respectively, and p the pressure. Using the continuity equation and the fact that flow is driven by pressure gradient in the z-direction, a fully developed inlet velocity profile for N number of fibers at $z = 0$ and $0 < r < r_b$ are obtained as [22]

$$u_r(r) = 0 \qquad \text{and} \qquad u_z(r) = \frac{2q_b}{N\pi r_b^4}\left(r_b^2 - r^2\right). \tag{2}$$

Here, q_b is the inlet blood flow rate in each of the hollow fibers with a fiber cross section area πr_b^2. Applying no slip condition at the wall and axisymmetric axis respectively at $r = 0$:

$$u_r = u_z = 0 \quad \text{and} \quad u_r = \frac{\partial u_z}{\partial r} = 0 \ \text{ at } r = 0;\ 0 \le z \le L. \tag{3}$$

The convection-diffusion equation governing the mass transport of solutes s coupled to the blood velocity field is given by

$$\overbrace{\frac{\partial c_s}{\partial t}}^{Transient} + \overbrace{u_z\frac{\partial c_s}{\partial z} + u_r\frac{\partial c_s}{\partial r}}^{\text{Convective Term}} = \overbrace{D_s\left(\frac{\partial^2 c_s}{\partial r^2} + \frac{1}{r}\frac{\partial c_s}{\partial r} + \frac{\partial^2 c_s}{\partial z^2}\right)}^{\text{Diffusive Term}} + \overbrace{B_s}^{\text{Buffer}} \tag{4}$$

where $c_s$and $D_s$are the concentration and the diffusion coefficient of solute $s$in the blood, respectively. The inlet and outlet boundary conditions for the concentration equation (4) are

$$c_s(z,r,0) = c_{s_0}, \quad c_s(0,r,t) = c_{s_0}, \quad \frac{\partial c_s(z,0,t)}{\partial r} = 0. \tag{5}$$

B_s defines the buffer term that vanishes everywhere except in the blood membrane domain and denotes the rate of solute s production or consumption per time. To help regulate blood bicarbonate concentration during HD therapy, a HCO_3^- based dialysate was employed in our model. Consideration was limited to water, hydrogen, and hydroxyl ions, and the CO_2 -containing species, CO_2, HCO_3^-, and H_2CO_3. We adapted buffer reaction rates of $s = [CO_2,\ HCO_3^-]$ given by [22] and [37]:

$$B_{CO_2} = -k_1\left(1 + \alpha\frac{2[CO_3^{2-}]}{[HCO_3^-]}\right)\left([CO_2] - \beta\frac{[HCO_3^-]}{[CO_3^{2-}]}\right), \tag{6}$$

$$B_{HCO_3^-} = -2B_{CO_2}, \tag{7}$$

where $\alpha = \frac{k_3K_2}{2k_1K_1}$, $\beta = \frac{k_{-1}K_1}{k_1}$ and $\frac{[HCO_3^-]}{[CO_3^{-2}]} = 20$ were calculated using the overall reaction equation (8), CO_2 and HCO_3^-reaction equations (9-11), and constants values in Table 1.

$$CO_2 + CO_3^{2-} + H_2O \leftrightarrow 2HCO_3^-, \tag{8}$$

$$CO_2 + H_2O \underset{k_{-1}}{\overset{k_1}{\rightleftharpoons}} H_2CO_3 \underset{k_{-2}}{\overset{k_2}{\rightleftharpoons}} H^+ + HCO_3^- \underset{k_{-3}}{\overset{k_3}{\rightleftharpoons}} H^+ + CO_3^{2-} \tag{9}$$

$$OH^- + CO_2 \underset{k_{-4}}{\overset{k_4}{\rightleftharpoons}} HCO_3^- \tag{10}$$

$$HCO_3^- \overset{K_1}{\rightleftharpoons} H^+ + CO_3^- \text{ and } H_2O \overset{K_2}{\rightleftharpoons} H^+ + OH^- \tag{11}$$

Table 1: Reaction and equilibrium constants and equations used in this paper at 297K

Table 1: Reaction and equilibrium constants and equations used in this paper at 297K

Constant	Value Equation	Unit	Ref
Reaction Constant, k_1	3.7×10^{-2}	s^{-1}	[22, 44, 51]
Reaction Constant, k_{-1}	1.4×10^{1}	s^{-1}	[22, 44]
Reaction Constant, k_3	8.5×10^{3}	$m^3 s^{-1} mol^{-1}$	[22, 44]
Reaction Constant, k_{-3}	2.0×10^{-4}	s^{-1}	[22, 44]
Density of Water, ρ_w	1.0×10^{3}	$kg\,m^{-3}$	[46]
Equilibrium Constant, K_1	$\exp[-12092.1/T - 36.786\ln T + 235.482]\rho_w$		[22, 51]
Equilibrium Constant, K_2	$\exp[1568.9/T - 2.5866 - 6.737\times10^{-3}T]$		[22, 51]

2.2. Trans-membrane Flow

The ultra-filtration flow passing through the dialyzer membrane (see Figure 2b) was described by K-K equations [45]

$$\begin{aligned} J_v &= L_p\Delta P - L_p RT\sigma\Delta c_s, \\ J_s &= C_s^*(1-\sigma)J_v + P_s\Delta c_s. \end{aligned} \tag{12}$$

J_v (m/s) is ultra-filtration velocity or volumetric flux across the membrane; J_s $(kg/m^2 s)$ is solute flux across the membrane; L_p (m/sPa) is hydraulic permeability of the membrane; P_s (m/s) is solute diffusive permeability coefficient of a membrane; R is gas constant; $T$is absolute temperature; σ is solute reflection coefficient. c_s^* (kg/m^3) represents the average solute concentration at each side of the membrane, Δc_s (kg/m^3) is solute concentration difference (i.e. trans-membrane concentration) across the membrane. The parameter ΔP (Pa) is the membrane surface hydraulic permeability of the membrane.

The permeability characteristics of the membrane were obtained from experiments where a dialysate flow was forced through the membrane. Hydraulic permeability described the volume of solution passing through unit membrane area, per unit pressure and time. Diffusive permeability related the amount of solute passing through unit area of membrane, per unit time and unit concentration difference across the membrane. Reflection coefficient described the fraction of solute that cannot pass through the membrane under specific flow conditions. Research have shown that when the fiber pore size is around 35 μm or more, σ is on the scale of 10^{-4}, which is very small [55]. Thus equation (12)

was further simplified to

$$\begin{aligned} J_v &\approx L_p \Delta P, \\ J_s &\approx C_s^* J_v + P_s \Delta c_s. \end{aligned} \tag{13}$$

Therefore, the ultra-filtration coefficient was calculated from the flow and transmembrane pressure measurements. Thus, the membrane interfacial conditions for the blood-side model were given by:

$$u_z = 0, \quad u_r = J_v\,, \tag{14}$$

$$D_s \frac{\partial c_s}{\partial r} = J_v c_s - J_s, \tag{15}$$

where volumetric flux, J_v, and solute flux, J_s, across dialyzer membrane were calculated using the simplified K-K equation (13).

2.3. Dialysate-Side Flow

Since each fiber was surrounded by a uniform annulus, as shown in Figure 3a, we adapted Krogh cylinder geometry [52] and [53] with annulus radius r_d which was far larger than the fiber radiusr_b. The transport of solutes in the annulus involved both convection and diffusion. By carefully controlling hydrostatic and osmotic pressures, we assumed that convection of the dialysate was not disturbed by the diffusion of solutes and determined only by the infusion pressure. Under these assumptions, the analytical solution of the dialysate velocity in the z-direction, u_z, was given by equation (18) with specified boundary conditions of $u_z = 0$ at $r = 0$ and $r = r_b$.

In addition, we adapted Frank et al. [43] dialysate inlet geometry where a raised collar with a small plate distributor was placed near the inlet (Figure 3a). The plate distributor was to prevent the dialysate from entering the fiber bundle directly. Thus, the inlet dialysate fluid would be impinged on the distributor, then goes around the collar and then penetrate into the fiber bundle. Similarly, the small plate distributor facing the outlet would cause the outlet dialysate to first flow out from the fiber bundle and then around the collar before going out. Therefore, we treated dialysate flow in both radial and axial directions. For simplicity, our dialysate computational domain involved only the plate distributors and the hollow fiber region in-between them (see Figure 3b).

Thus, the control concentration equation for the dialysate side can be described

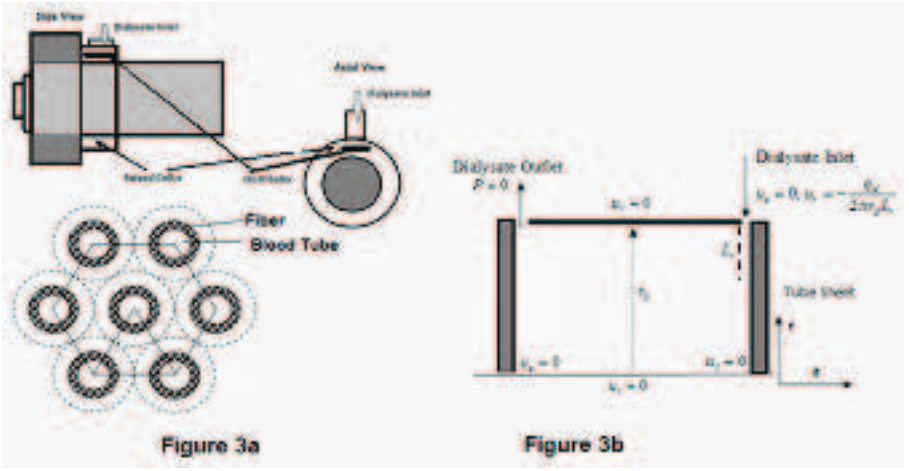

Figure 3: Geometric configuration near dialysate inlet. The distributors are designed to keep the dialysate entering the hollow fibers uniformly. (b) Schematic computational domain at the dialysate compartment.

in similar form as equation (4):

$$\overbrace{\frac{\partial c_s}{\partial t}}^{\text{Transient}} + \overbrace{u_z\frac{\partial c_s}{\partial z} + u_r\frac{\partial c_s}{\partial r}}^{\text{Convective}} = \overbrace{D_s\left(\frac{\partial^2 c_s}{\partial r^2} + \frac{1}{r}\frac{\partial c_s}{\partial r} + \frac{\partial^2 c_s}{\partial z^2}\right)}^{\text{Diffusive}} + \overbrace{R_s}^{\text{Replenishment}}, \quad (16)$$

with a fully developed axial and radial velocities [35] and [56]:

$$u_r(r_b) = -\frac{q_d}{2\pi r_b L_r} \qquad \forall\ r_b, \quad (17)$$

$$u_z = \frac{2q_d}{\pi r_d^2 L_r}\frac{\ln(r/r_d) - ((r/r_d)^2 - 1)/(k^2-1)\ln(k)}{(k^2+1)\ln(k) + 1 - k^2}. \quad (18)$$

Here, the parameter q_d represented flow rate in the dialysate inlet, $k$the ratio of r_b/r_d, and L_r the width of the raised collar. The solute replenishment term, R_s, was introduced to help maintain dialysate concentration level and was calculated using [22]

$$R_s = \varepsilon c_s(c_{s_0} - c_s), \quad (19)$$

where $\varepsilon$is the replenishment coefficient.

3. Algorithm, Technique, and Parameters

3.1. Algorithm and Techniques

The governing equations (4) and (16) and their initial and boundary conditions (2-3), (5-7), (13-15), (17-19) were converted into non-dimensional forms using the same scale factors for both blood and dialysate flow regions. The non-dimensional variables indicated with superscript '*' in equation (20) and the reference variables given in Table 2.

$$\begin{array}{l} r^* = \frac{r}{L};\ \ z^* = \frac{z}{L};\ \ u_r^* = \frac{u_r}{U};\ \ u_z^* = \frac{u_z}{U};\ \ A_1 = \frac{k_1 L}{U};\ \ Sh_s = \frac{LP_s}{D_s}; \\ c_s^* = \frac{c_s}{c_{s_0}};\ \ t^* = \frac{tU}{L};\ \ \phi = \frac{r_b}{L};\ \ Pe = \frac{LU}{D_s};\ \ Re = \frac{\rho U r_b}{\mu};\ \ E_s = \frac{\tilde{L}_p L \Delta p}{2D_s}; \end{array} \tag{20}$$

The dimensionless parameters Pe and ϕ define the Peclet number and Aspect ratio respectively. $Pe = LU/D_s = q_b/\pi r_b D_s$ expressed the relative importance of convection to diffusion while $Re = \rho U r_b/\mu = \rho q_b/\mu r_b$ related inertial effects to viscous effects. Since dialysis devices employ laminar fluids flow with $Re << 1$ the inertial effects would be irrelevant. Therefore, it would not explicitly appear affecting inertia in the flow equations [54].

Substituting the dimensionless variables in (20) into equation (4) or (16) and dropping the superscript '*' resulted in

$$\frac{\partial c_s}{\partial t} + u_z \frac{\partial c_s}{\partial z} + u_r \frac{\partial c_s}{\partial r} = \frac{1}{Pe}\left(\frac{\partial^2 c_s}{\partial r^2} + \frac{1}{r}\frac{\partial c_s}{\partial r} + \frac{\partial^2 c_s}{\partial z^2}\right) + \psi_s, \tag{21}$$

where ψ_s defined the dimensionless buffer or the replenishment term.

Symbol	***Description***
$\boldsymbol{L}$	Reference length: They are the same for both compartments.
U	Reference Velocity
c_{s_0}	Reference solute concentration

Table 2: The reference variables with their description

The dimensionless initial and boundary conditions corresponding to equation (21) were

Blood-Side Inlet Velocity Conditions:

$$u_r = 0 \quad \text{and} \quad u_z = \frac{2q_b}{N\pi r_b^2 U}\left(1 - \frac{r^2}{\phi^2}\right) \tag{22}$$

Dialysate-Side inlet and outlet velocities:

$$\begin{aligned} u_r &= -\tfrac{q_d}{2\pi r_b U L_r} \qquad \forall r_b \\ u_z &= \tfrac{2q_d}{\pi r_d^2 U L_r}\left(\tfrac{\phi^2(k^2-1)\ln(k)\cdot[\ln(kr)+\ln(\phi)]-[(kr)^2-\phi^2]}{(k^2-1)\ln(k)\cdot[(k^2+1)\ln(k)+1-k^2]}\right) \end{aligned} \tag{23}$$

No slip and axisymmetric conditions:

$$u_r = u_z = 0, \text{ and } u_r = \frac{\partial u_z}{\partial r} = 0 \text{ at } r = 0; \ 0 \le z \le 1. \tag{24}$$

Inlet and outlet blood and dialysate concentrations:

$$c_s(z, r, 0) = 1, \quad c_s(0, r, t) = 1, \quad \frac{\partial c_s(z, 0, t)}{\partial r} = 0. \tag{25}$$

Buffer and Replenishment terms:

$$\psi_{CO_2} = -A\left([CO_2] - 20\beta\right)\left(1 + 2\alpha\frac{[CO_3^{2-}]}{[HCO_3^-]}\right); \ \psi_{HCO_3^-} = -2\psi_{CO_2}, \tag{26}$$

$$\psi_{R_s} = \frac{\varepsilon c_{s0} L}{U} c_s(1 - c_s), \tag{27}$$

where ψ_{CO_2} and $\psi_{HCO_3^-}$ represented dimensionless buffer terms in blood-side and ψ_{R_s} depicted dimensionless replenishment term for solute $s = CO_2$ and HCO_3^-.
Blood-Membrane interfacial conditions:

$$u_z = 0, \quad u_r = \frac{J_v}{U} = \frac{E_s}{Pe_s}, \quad \frac{\partial c_s}{\partial r} = E_s(1 - C_s^*) - Sh_s \cdot \Delta c_s, \tag{28}$$

where Sh_s is the Sherwood number and E is the ratio of momentum and mass diffusivity defined in (20).

The dimensionless forms of (21) were solved numerically by using Finite Volume Method (FVM) subject to the boundary and initial conditions (22-28). This method discretized the model system by integrating (21) over a finite volume and then applying the divergence theorem. Application of FVM resulted in the creation of grid structures such that the number of rectangular cells in $r-$ and $z-$directions remained constant throughout the domain of interest. However, the grid size was made to vary, although strong variations in grid size could affect the accuracy [42]. For the spatial domain the numerical model used separate sub-domain grids for blood and dialysate models since domain dimensions were different.

Since the model equations provided no direct means for pressure-velocity coupling, a semi-implicit method for pressure linked equations (SIMPLE) method

was used for pressure coupling. The velocity distributions were calculated with a Picard iteration method using stabilized bi-conjugate gradient with a tolerance of 10^{-8}. Hybrid Differencing Method based on central and upwind differencing was used numerically to discritize the diffusion terms. The method switches to upwind differencing when the central differencing produces inaccurate results at high Peclet numbers.

The concentration equations were solved using Picard iteration with a tolerance of 10^{-8}. In order to account for the diffusivity differences between the blood and dialysate sides, boundaries of the domain of interest were chosen at the faces of the rectangular control volumes, rather than at its grid points. Therefore, following the approach of Versteeg et al. [42], one extra grid row or column outside the boundary was allowed for easy application of the boundary conditions. Furthermore, since some of the boundary conditions depended on values in adjacent grid points and the model equations only defined the values in the interior of the domain, the boundary conditions were definable in terms of grid values to the interior of that boundary.

Thus, the simulation methodology for our model was to solve for pressure and velocity equations in blood and dialysate compartments. The pressure and velocity calculated was then used to compute the concentration distributions in both blood and dialysate compartments. At each grid on the membrane surface ΔP was calculated first, then computed J_v and J_s using K-K equations. The pressure and concentration calculated were then transferred to K-K equations as boundary conditions to calculate TM fluxes of carbon dioxide and bicarbonate solutes. The TM fluxes values were used to calculate the replenishment term (R_s) and then used as the boundary conditions in the model system to generate the next iteration.

3.2. Parameters

In this simulations, blood and dialysate inlet bicarbonate concentrations were set to 19 $mol \cdot m^{-3}$ and 35 $mol \cdot m^{-3}$ respectively, while the blood-side and dialysate-side flow rates were respectively, 350 mL/min (i.e. $5.83 \times 10^{-6}\ m^3 s^{-1}$) and 800 mL/min ($1.33 \times 10^{-5}\ m^3 s^{-1}$), [7, 22, 35]. Parameters and constant values used in this paper are listed in Table 3. Others not shown in this table were variables or parameters computed using values in Table 3.

Parameter (Unit)	***Symbol***	***Value***	***Ref***
Diffusion coefficient of CO_2 in Blood (m^2s^{-1})	$D_{CO_2,b}$	$3.4 * 10^{-10}$	[22], [35]
Diffusion coefficient of HCO_3 in Blood (m^2s^{-1})	$D_{HCO_3,b}$	$1.4 * 10^{-10}$	[22], [35]
CO_2Diffusion coefficient in dialysate (m^2s^{-1})	$D_{CO_2,d}$	$1.59 * 10^{-9}$	[22], [36]
HCO_3^-Diffusion coefficient, dialysate (m^2s^{-1})	$D_{HCO_3,d}$	$1.18 * 10^{-9}$	[22], [36]
Membrane effective length (m)	L	0.22	[32], [50]
Hydraulic Permeability (m/sPa)	L_p	$1.2 * 10^{-10}$	[32]
Width of raise collar (m)	L_r	0.014	[32]
Fiber diameter (μm)	L_f	200	[32], [50]
Fiber thickness (μm)	e	40	[50]
Number of fibers	N	9000	F60
Membrane permeability of CO_2 (ms^{-1})	P_{CO_2}	$1.72 * 10^{-9}$	[35], [36]
Membrane permeability of $HCO_3(ms^{-1})$	$P_{HCO_3^-}$	$1.95 * 10^{-9}$	[35], [36]
Radius of dialysate channel (m)	r_d	$1.25 * 10^{-4}$	[50],[51]
Radius of blood channel (m)	r_b	2.0×10^{-4}	[50],[51]
Initial velocity at blood inlet (ms^{-1})	u_b	$1.73 * 10^{-2}$	[50], [52]
Initial velocity at dialysate inlet (ms^{-1})	u_d	$1.21 * 10^{-2}$	[50], [52]

Table 3: Geometric and transport characteristics of hollow fiber module used

4. Results and Discussions

For the purpose of the applicability of our model system, we made numerical illustrations of all physical parameters involved in the model analysis. The computations performed estimated quantitatively the profiles of the velocity fields, trans-membrane pressures, ultra-filtrations, and solute fluxes in both blood and dialysate compartments. We first tested the grid independence of the mesh scheme used in our simulation by generating UF velocities on meshes of 10 x 100, 15 x 150, and 20 x 200 respectively. The resulted output, Figure 4a, showed a well fitted plot of different meshes. Thus, we used 20 x 200 mesh in

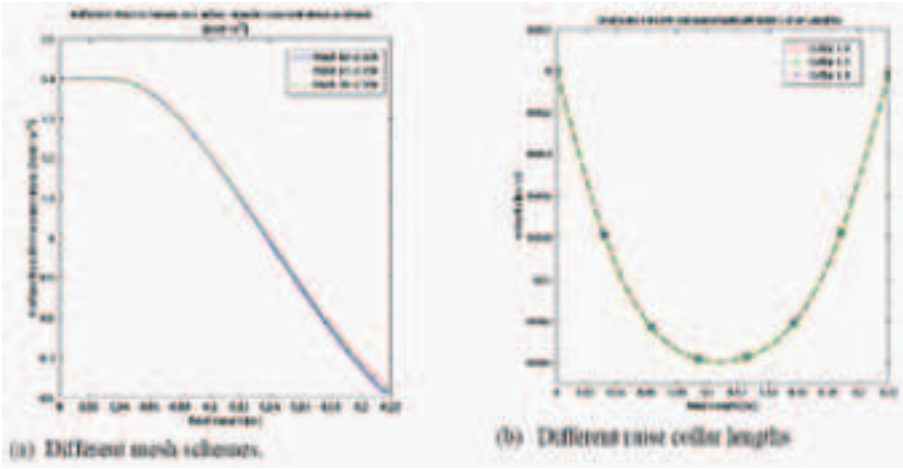

Figure 4: (a) Comparison of different mesh schemes on carbon dioxide concentration in the membrane. The results showed well fitted meshes so a mesh dimension of 20 x 200 was used in this paper. (b) The results of different collar lengths were all fitted. Our simulations use collar length 1.4 meters.

our simulation in each semi-compartment for the quantities of interest displayed in this paper.

Different raised collar lengths were tested in the dialysate compartment since that compartment is notorious for non-uniform flow distribution, shown in Figure 4b. The converged results for a raised collar length of 1.4 cm for various quantities were illustrated through Figures 5-14.

4.1. Flow Profiles of Velocity, Ultra-Filtration, and Pressure in Blood and Dialysate Compartments

The velocity profiles at blood and dialysate compartments were shown in Figures 5-14. In Figure 5a, the blood-side axial velocity contour showed a uniform flow across each hollow fiber. The result was contrary to Ronco et al. [17] observation when Computerized Helical Scanning Technique was used to observe a non-uniform blood flow distribution in hollow fibers. Our result may suggest that the new blood header design used in modern hollow-fiber dialyzers is an efficient flow distributor. The axial blood side velocity at different time periods and both axial and average blood-side velocity profiles were shown in Figures 5b and 6a, respectively. At different time periods, the axial velocity remained

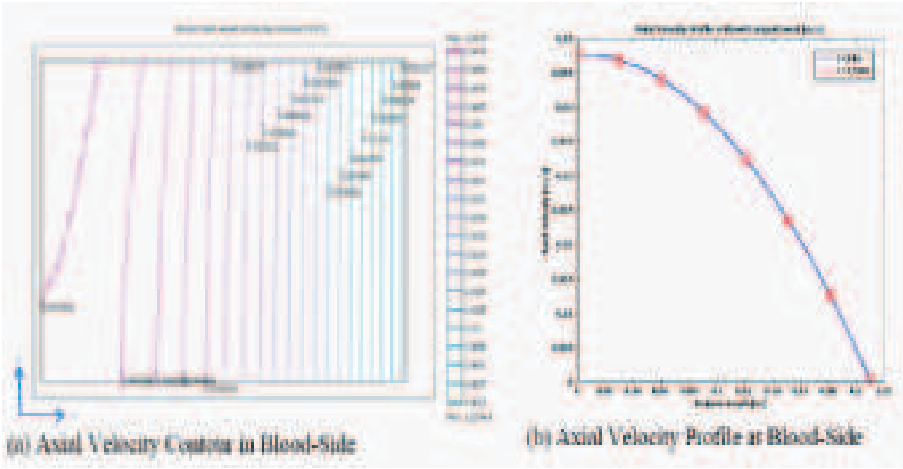

Figure 5: (a) Shows velocity contour map in the blood compartment in axial and radial directions. (b) Shows axial velocity profiles inside the blood compartment at different time periods along the axial direction with axial length 22 cm.

uniform across the fiber length. The parabolic nature of the velocity profiles in Figure 5b decreased from the maximum value of $0.0478\,ms^{-1}$ along the axial direction and finally approached a minimum value of $0.00123\,ms^{-1}$at the wall of the compartment. It was noted that the axial velocity profile inside the blood compartment is the same as the average of all the velocity distributions within each cross-section of the fiber length (see Figure 6a). Thus, the axial velocity profile represented a localized average of the speed in the blood compartment. The decreased in velocity flow within the blood compartment observed may be caused by the geometry of blood inlet and UF loss along the axial length.
The blood-side velocity flow patterns in the radial direction at various axial lengths still showed parabolic in shape. However, the velocity got enhanced with an increased in axial length over almost the entire radial region, as shown in Figure 6b.

Unlike the nature of the axial velocity profile of the blood flow, the radial velocity component showed heterogeneity in nature, Figure 7.

The heterogeneity nature may be caused by the fibers elongated along the axial length or suspected non-uniformity in the dialyzer inlet blood flow. Thus, the radial inflow together with the internal helicoidally distributor did not promote homogeneous access to all fibers. Therefore, for better blood flow, further

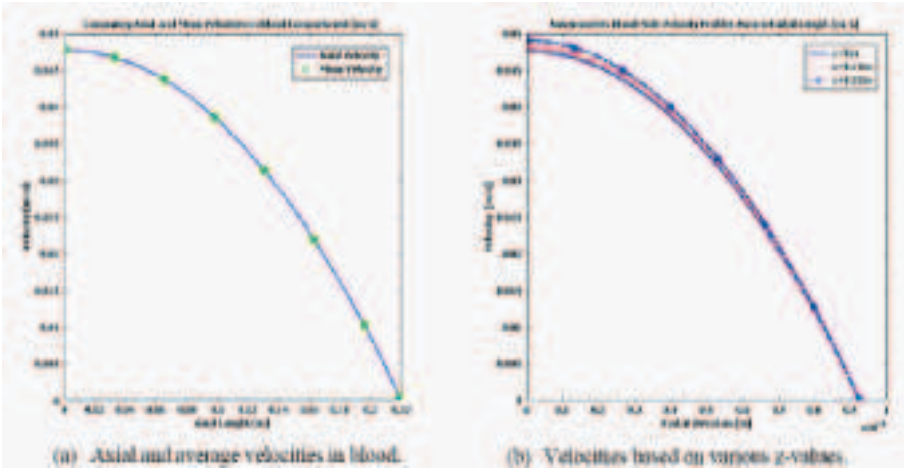

Figure 6: (a) Blood-Side axial velocity profile of dialyzer of length 22 cm. Blood flow rate is 350 mL/min. The flow is uniform across each cross-section of the fibers. The non-steady state velocity profile represents a localized average of the speed in the blood-fiber bundle compartment. (b) Blood compartment velocity profiles at different axial locations along the radial direction.

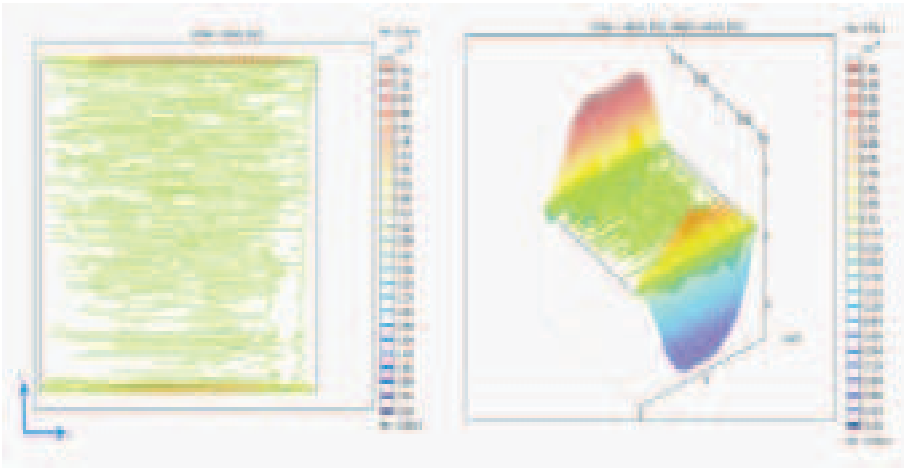

Figure 7: Radial velocity contour map in blood-side showed heterogeneity pattern. The velocity flows were much higher at the dialyzer's inlet and the fibers elongation.

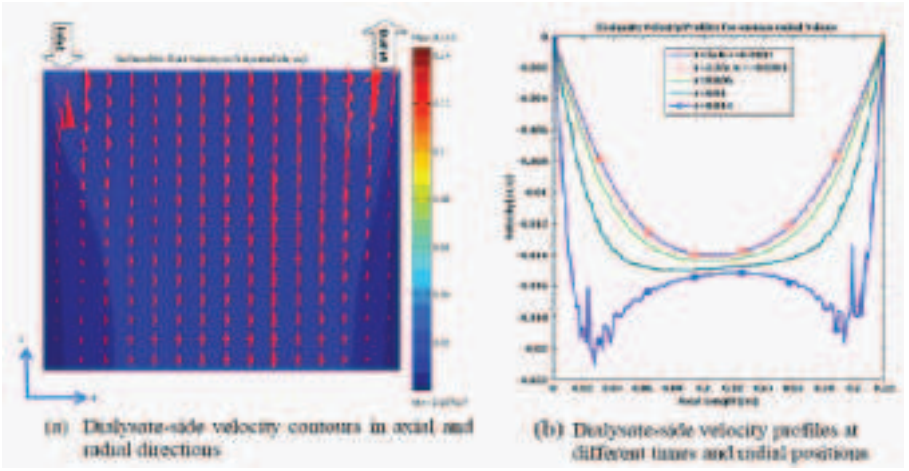

Figure 8: (a) Velocity field distribution inside dialysate compartment indicated radial velocity dominants in the dialysate inlet and outlet, while the axial velocity was strong in the middle. The strength of the arrow indicated both magnitude and direction of the dialysate velocity. (b) Velocity profiles at different time periods and radial positions along the axial length were shown. The dialysate flow rate of 800 mL/min at room temperature was used for the simulation.

investigation needed to be conducted.

Figure 8 represented the respective velocity contour map and profiles inside dialysate compartment. The axial flow velocity was dominant in the central region while the radial flow velocity was significant in dialysate inlet and outlet areas, as shown in Figure 8a. The dialysate flow near the inlet and outlet ports were observed to be non-uniformed in nature. The dialysate velocity profiles for various radial positions presented in Figure 8b showed an all time negative along the axial length. The velocity profiles declined from zero as one moves away from $z = 0$ and attained their maxima at a short distance away from it. They eventually increased to zero again towards the end of the axial length. The pulsatile nature of the velocity profiles reflected the non-uniform behavior in the dialysate compartment. When the radial length was increased, the velocity profile got perturbed more, as shown in Figure 8b.

The non-uniformity of the dialysate flow distribution suggested that the collars used in existing hollow fiber dialyzers to help dialysate uniform flow failed to promote uniform dialysate flow. Consequently, the non-uniformity of flow distribution may result in non-uniform solute concentration distribution

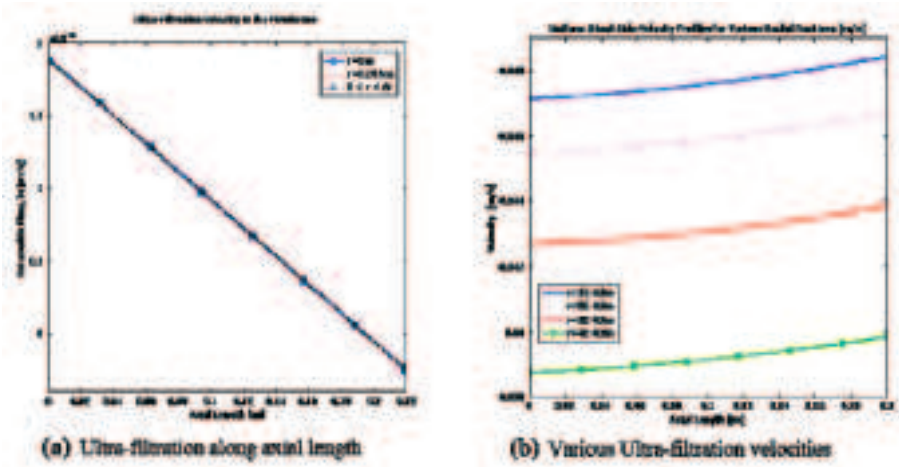

Figure 9: Ultra-filtration velocity and solute flux profiles along the axial membrane length

in dialysate compartment. Since solute exchange across dialyzer membrane is influenced by blood and dialysate flow velocity and concentration, we expect inefficient exchange of solutes at the membrane level.

Figure 9a showed the ultra-filtration velocity (J_v) profile along the dialyzer membrane. In general, the profile decreased from the blood-side inlet to its outlet with positive ultra-filtration velocity along the greater part of the membrane.

Various ultra-filtration velocities at different radial positions were presented in Figure 9b. The profiles were rising from the inlet of the blood compartment to its outlet. The smaller the dialyzer membrane width, the larger the ultra-filtration velocity profile in the membrane.

As a result of the small ultra-filtration flow permeating through the membrane, the pressure profile at the blood-side dropped linearly along the axial length from 25 kPa to zero as presented in Figure 10a. However, the dialysate-membrane pressure profile, presented in Figure 10b, increased from 1.0 kPa to 3.7 kPa and deviated slightly from linearity. Since both blood-membrane and dialysate-membrane pressures along the axial length were nearly linear, the trans-membrane pressure shown in Figure 11a was also slightly linear. This resulted in a nearly linear ultra-filtration velocity profile in the membrane.

As a result of local variation of trans-membrane pressure and blood pressure loss through the hollow fiber pathway, back-filtration might occur (see Figure 11b). Back-filtration problem is very critical during dialysis session as it induces

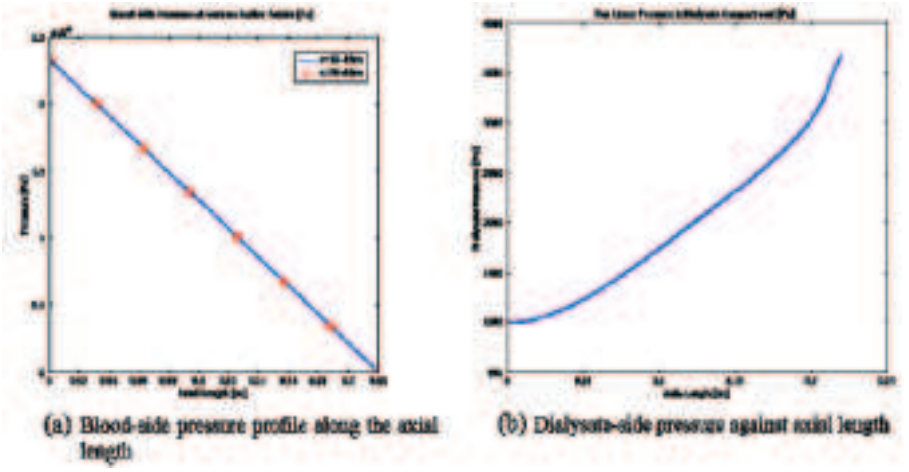

Figure 10: The pressure profiles in blood and dialysate compartments. (a) Showing blood-side pressure dropping linearly along the axial length from 25 kPa to zero. (b) Shows dialysate-side pressure increasing from 1.0 kPa to 3.7 kPa and deviating slightly from linearity.

contamination into the blood. In our model, back-filtration occurred as a result of reversed osmosis. Specifically, the hydraulic trans-membrane pressure could not overcome the trans-membrane osmotic pressure.

In Figure 12, solute flux (J_s) for $s = HCO_3^-$, along the membrane surface was observed to increase sharply initially as the axial distance is increased. The rising profile indicated that the TM concentration ($\triangle\ c$) at the blood-side outlet region was significantly higher than that at the inlet region. The solute flux profile then became nearly uniform along the membrane surface. The negative values showed back-filtration possibly caused by reverse osmoses. The variation between J_s and J_v (see Figures 11a and 12) indicated that there was an increase of bicarbonate solute in the membrane. Thus, bicarbonate solute flux was more influenced by the TM concentration ($\triangle\ c$) between the blood and dialysate sides of the membrane.

4.2. Boundary and Bulk Bicarbonate Concentrations

The boundary and bulk HCO_3^- concentration distributions at blood compartment across axial length were shown in Figure 13a. As observed, the boundary and bulk HCO_3^- concentrations at the exit point were almost identical and

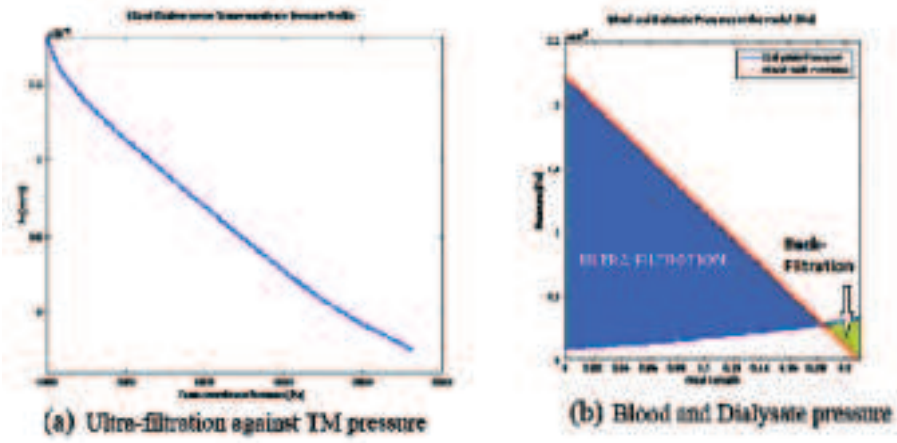

Figure 11: (a) Ultra-filtration profile plotted against the trans-membrane showing a decreasing route. (b) Both blood- and dialysate-side pressure difference depicting ultra-filtration and back filtration across the membrane.

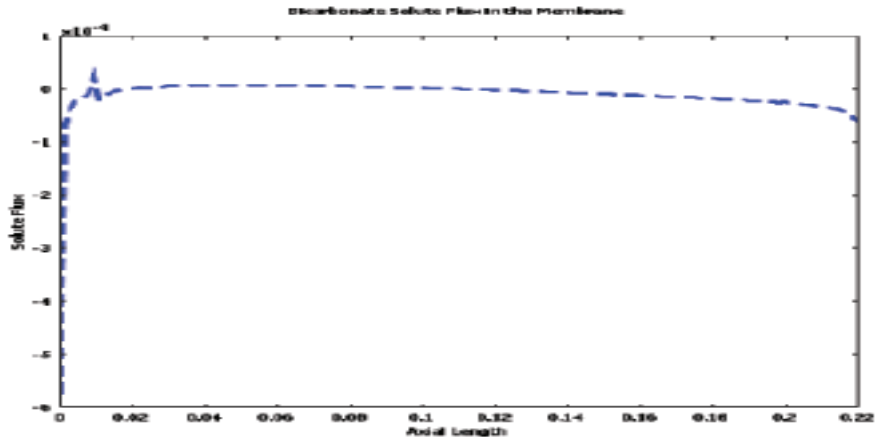

Figure 12: Bicarbonate flux profile across the membrane surface increasing sharply initially and the becoming nearly uniform. Negative values indicating back-filtration caused by reverse osmoses in the membrane.

stable. This was crucial since the bulk concentration level actually enters the patients' body and might put the patient at risk of bicarbonate overdose if it is not within the physiologic range and identically stable. However, the observed

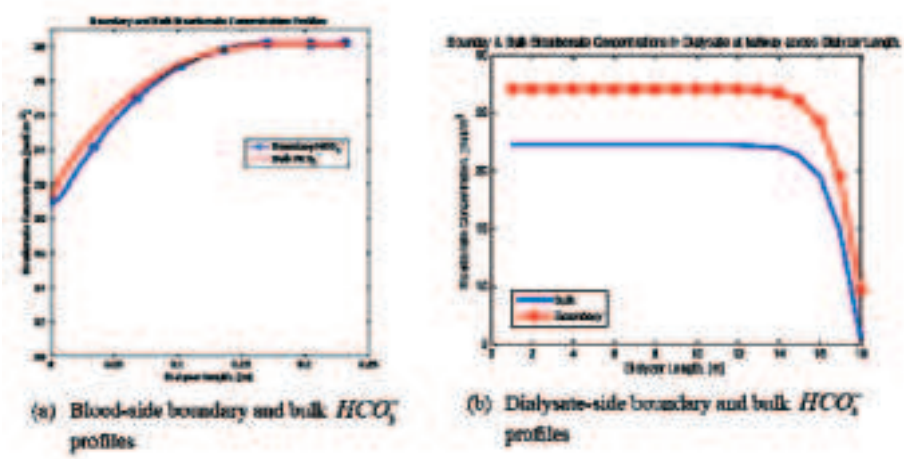

(a) Blood-side boundary and bulk HCO_3^- profiles

(b) Dialysate-side boundary and bulk HCO_3^- profiles

Figure 13: (a) Boundary and bulk concentration profiles of bicarbonate in the blood as a function of dialyzer length during dialysis session. Both boundary and bulk HCO_3^- concentrations at the exit point were almost identical, stable, and within the physiologic range of 28-30 $mol \cdot m^{-3}$. (b) Boundary and bulk bicarbonate concentrations plot across the dialyzer length in the dialysate compartment. The boundary bicarbonate concentration is observed to be higher than the bulk bicarbonate concentration.

bulk HCO_3^- inlet concentration was not 19.0 $mol \cdot m^{-3}$ (value we started with), but 19.7 $mol \cdot m^{-3}$. This discrepancy maybe caused by the incomplete dissociation of carbonic acid (H_2CO_3) into HCO_3^- and H^+, suggesting a bicarbonate ions carryover effect. Nevertheless, both boundary and bulk HCO_3^- ions in blood compartment were within the physiologic range (28 - 30 $mol \cdot m^{-3}$) and significantly more than the pre-dialysis HCO_3^- value.

However, boundary and bulk HCO_3^- concentrations in dialysate side toward the hollow-fibers were stable but not identical. As observed in Figure 13b, the boundary HCO_3^- concentration was between 28-30 $mol \cdot m^{-3}$ and was more than the bulk bicarbonate concentration (24-26 $mol \cdot m^{-3}$). The amount of HCO_3^- concentration lost in the dialysate could be (i) transferred into the patient blood or captured inside the hollow-fibers membrane, (ii) consumed by chemical reactions between HCO_3^- and other solutes in the dialysis fluid, and (iii) other unknown phenomena.

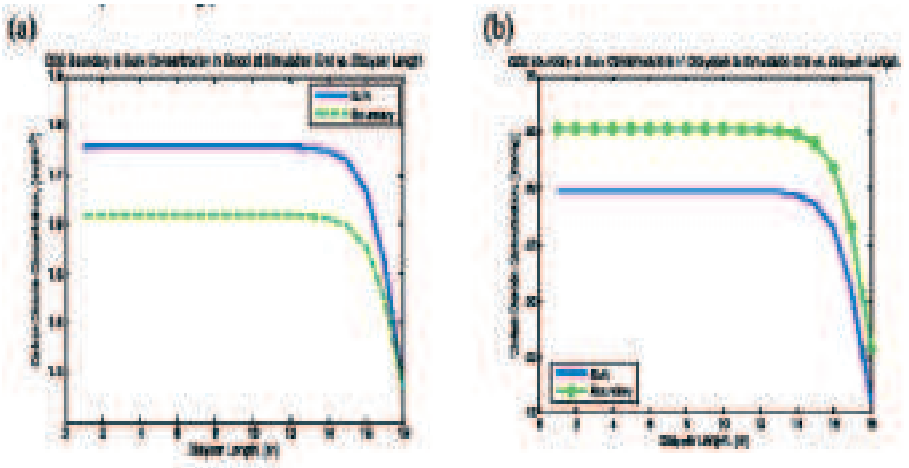

Figure 14: (a) Boundary and bulk carbon dioxide concentrations plotted along the dialyzer length in the blood compartment. Bulk carbon dioxide concentration is higher than the boundary concentration because carbon dioxide is transferred from dialysate to the blood during dialysis session. (b) Boundary and bulk carbon dioxide concentrations in partial pressure verses dialyzer length.

4.3. Boundary and Bulk Carbon Dioxide Concentrations

Both boundary and bulk CO_2 concentrations in the blood increased along the axial length (see Figure 14a). However, the bulk CO_2 concentration was higher than the boundary CO_2 concentration. This observation confirmed Sombolos et al. (2005) conclusion that CO_2 always get transferred from dialysate to blood during dialysis session. The concentration of dissolved CO_2 increased by 37.%, (1.28-1.76$mol \cdot m^{-3}$) after dialysis therapy.

The boundary and bulk CO_2 concentrations in dialysate (shown in Figure 14b) represented concentrations towards the hollow-fibers in partial pressure. Contrast to CO_2 concentration in the blood, the boundary CO_2 in dialysate was higher than that of bulk concentration. This might resulted from CO_2 infusion in the closed dialysis system and therefore caused an average CO_2 partial pressure (pCO_2) of 62 mmHg in the dialysate inlet. Since the relationship between pCO_2 and its concentration in our simulation was $[CO_2] = 0.0307 * pCO_2$, it provided a dissolved CO_2 concentration of 1.90 $mol \cdot m^{-3}$ at the dialysate inlet.

5. Conclusion

Numerical results showed a uniform flow profiles in blood compartment and a non-uniform flow profiles near the hollow-fibers at the dialysate side. This non-uniformity suggested that the collars used in modern hollow-fiber dialyzers to help achieve uniform dialysate flow failed to promote dialysate uniformity. Consequently, the flow mismatch at blood and dialysate sides may affect solute transfer across the membrane since exchange of solutes at the membrane level depends on solute concentration and flow characteristics. The effects of TM pressure on J_v and J_s through the membrane were also examined in detail. The variation between J_s and J_v indicated an increase of small solute (e.g. bicarbonate) in the membrane. The pressure and concentration profiles were also detailed and analyzed. Variation of TM pressure and blood pressure loss through the membrane pathway caused BF. Further analysis on boundary and bulk solutes depicted uniform and stable profiles in the membrane and non-uniform in the dialysate. Thus, the mismatch flow characterized at blood and dialysate ends may affect diffusivity of small fluxes as reported by clinical studies [22-25]. Thus, the proposed model gave insight of dialysis flow characteristics during therapy session and may open the possibilities for the design or modification of high efficient hollow-fiber dialyzer or blood filtration systems.

Acknowledgments

This work was partially funded through graduate teaching assistantship by the Department of Mathematics and Statistics, University of Vermont. The author also wishes to express his thanks to Minot State University for allowing him to use their Resource.

References

[1] Sakai K. Technical Determination of Optimal Dimension of Hollow Fibre Membranes for Clinical Dialysis. Nephrol Dial Transplant 4 (1989) [Suppl]: S73-S77.

[2] Sigdell JE. Calculation of Combined Diffusive and Convective Mass Transfer. Int. J. Artif. Organs (1982), 5:361-72.

[3] Takesawa S, Terasawa M, Sakagami M, Kobayashi T, Hidai H, Sakai K. Nondistructive Evaluation by X-Ray Computed Tomography of Dialysate

Flow Patterns in Capillary Dialyzers. ASAIO Tran., 34, (1988), pp 794-799.

[4] Vander Velda C, Leonard EF. Theoretical Assessment of the Effect of Flow Maldistributions on the Mass Transfer Efficiency of Artificial Organ. Med. Biol. Eng. Comp. (1985), 23:224-229.

[5] Ledebo I. Principles and Practice of Hemofiltration and Hemo diafiltration. Articial Organs 1998. 22(1):20-25.

[6] Port FK, Orzol SM, Held PJ, Wolfe RA. Trends in Treatment and Survival for Hemodialysis Patients in the United State. Am. J. Kidney Dis. 32 (1998) (Suppl. 4): s34-s38.

[7] Gennari FJ. Acid-Base Considerations in End Stage Renal Disease. In: Henrich WL ed. Principles and Practice of Dialysis. Philadephia, PA: Lippincott Williams & Wilkins, (2004) 393-407.

[8] Haitham H, Eathar R, Samir S. Effect of End-Stage Renal Failure and Hemodialysis on Mortality Rates in Implantable Cardiovester-Defibrillator Recipients, 2007.

[9] Sarnak MJ, Levey AS. Epidemiology of Cardiac Disease in Dialysis Patients: Uremia-Related Risk Factors, Seminars in Dialysis (1999) 12:69-76.

[10] U.S. Renal Data System: USRDS 2002 Annual Data Report, in, Bethesda, MD, The National Institutes of Health, National Institute of Diabetes and Digestive Diseases, 2002.

[11] Levin A. Clinical epidemiology of cardiovascular disease in chronic kidney disease prior to dialysis, Semin. Dial. (2003); 16(2):101-5.

[12] Kulz M, Nederlof B, Schneider H. In vitro and In vivo Evaluation of a New Dialyzer, Nephrol Dial Transplant (2000) 17: 1475-1479.

[13] Streicher E, Schneider H. The Development of a Polysulfone Membrane. Contr Nephrol (1985); 46: 1-13.

[14] Ronco C, Ballestri M, Brendolan A. New Developments in Hemodialyzers. Blood Purif (2000); 18: 267-275.

[15] Woffindin C, Hoenich NA. Hemodialyzer Performance: a Review of the Trends over the Past Two Decades. Artif Organs (1995); 19:1113-1119.

[16] Clark W, Rocha E, Ronco C. Solute Removal by Hollow-Fiber Dialyzers, Contrib Nephrol, Basel, Karger, (2007), vol 158, pp 20-33.

[17] Ronco C, Brendolan A, Crepaldi C, Rodighiero M, Scabardi M. Blood and Dialysate Flow Distributions in Hollow-Fiber Hemodialyzers Analyzed by Computerized Helical Scanning Technique. J Am Soc. Nephrol (2002) 13:s53-61.

[18] Ronco C, Breuer B, Bowry SK. Hemodialysis Membranes for High-Volume Hemodialytic Therapies: The Applications of Nanotechnology. Hemodialysis Int., (2006), 10:s48-s50.

[19] Agishi T, Ota K, Nose Y. Is Hollow Fiber Occlusion Due to Maldistributions of Blood? Proc. Eur. Dial. Transplant Assoc., 12, (1975), pp 519-525.

[20] Ronco C, Levin N, Brendolan A, et al. Flow Distribution Analysis by Helical Scanning in Polysulfone Hemodialyzers: Effects of Fiber Structure and Design of Flow Patterns and Solute Clearances. Hemodialysis Int., (2006); 10: 380-388.

[21] Zhang J, Parker DL, Leypoldt JK. Flow Distribution in Hollow Fiber Hemodialyzers Using Magnetic Resonance Fourier Velocity Imaging, ASAIO J. 41, (1995), pp M678-682.

[22] Annan K. Mathematical Modeling of the Dynamic Exchange of Solutes during Bicarbonate Dialysis. Mathematical and Computer Modelling 55 (2012), 1691-1704.

[23] Poh CK, Hardy PA, Clark WR, Gao D. Characterization of Flow in Hemodialyzers Using MRI: Proceedings of International Society of Magnetic Resonance in Medicine, 9, (2002), pp 1984,.

[24] Poh CK, Hardy PA, Liao Z, Huang Z, Clark WR, Gao D. Nonintrusive Characterization of Fluid Transport Phenomina in Hollow Fiber Membrane Modules Using MRI: An Innovative Experimental Approach, in New Insights into Membrane Science Technology: Polymeric, Inorganic, and Biofunctional Membranes, edited by Bhattacharyya D, Butterfield A, Elsevier Science, Amsterdam, UK, 2003

[25] Ronco C, Breuer B, Bowry SK. Hemodialysis Membranes for High-Volume Hemodialytic Therapies: The Applications of Nanotechnology. Hemodialysis Int., (2006), 10:s48-s50.

[26] Nordon RE, Schindhelm K. Design of Hollow Fiber Modules for Uniform Shear Elution Affinity Cell Separation. Artif. Organs 21: (1997) 107-115.

[27] Burgelman M, Vanholder R, Fostier H, Beigair S. Estimation of Parameters in a two-pool Urea Kinetic Model for Hemodialysis. Med. Eng. Phys. (1997) 19:69-76.

[28] Kopple JD, Jones MR, Keshaviah PR, Bergstrom J, Lindsay RM, Moran J, Nolph KD. A proposed Glossary for Dialysis Kinectics. Am J Kidney Dis. (1995), 26:963-981.

[29] Maasrani M, Jaffrin MY, Fischbach M, Boudailliez B. Urea Creatinine and Phosphate Kinectic Modeling During Dialysis: Application to Pediatic Hemodialysis. Aritif. Kidney Dial. (1995), 18:122-129.

[30] Schneditz D, Fariyike B, Osheroff R, Levin MW. Is Intercompartmental Urea Clerance during Hemodialysis a Perfusion Term? A Comparison of two pool Urea Kinetic Models. J Am. Soc. Nephrol (1995) 6:1360-1370.

[31] Hakim RM, Depner TA, Parker TF. Adequacy of Hemodialysis. Am. J. Kidney (1992) Dis. 20:108-122.

[32] Depner TA. Prescribing Hemodialysis. New York, Kluwer Acedemic Publishers, 1991.

[33] Gotch FA. Kinetic Modeling in Hemodialysis, in Clinical Dialysis, edited by Nissenson AR, Fine RN, Gentile D, Norwalk, Appleton and Lange, (1990), pp 118-146.

[34] Cooney DO, Kim SS, Davis EJ. Analyses of Mass Transfer in Hemodialyzers for Laminar Blood Flow and Homogeneous Dialysate, Chem. Eng. Sci., 29 (1974) 1731-1738.

[35] Liao Z, Poh CK, Huang Z, Hardy PA, Clark WR, Gao D. A numerical and experimental study of mass transfer in the artificial kidney. J. Biomech. Eng. (2003); 125(4):472-80.

[36] Maren TH. Chemistry of the Renal Reabsorption of Bicarbonate. Can. J. Physiol. Pharmacol. (1974), 52:1041.

[37] Suchdeo SR and Schultz JS. Permeability of Gases through Reacting Solutions: The Carbon Dioxide – Bicarbonate Membrane System, Chem. Eng. Science, (1974), Vol. 29 pp. 13-23.

[38] Petersen J, Hyver SW, Cajias J. Backfiltration During Dialysis: A Critical Assessment, Seminars in Dial., (1992) Vol 5: 1, pp13-16.

[39] Ronco C, Brendolan A, Feriani M et al. A New Scintigrapgic Method to Characherize Ultrafiltration in Hollow Fiber Dialyzers. Kidney Int (1992); 41: 1383-1393.

[40] Leypoldt JK, Schmidt B, Gurland HJ. Net Ultrafiltration May Not Eliminate Backfiltration During Hemodialysis with Highly Permeable Membranes, Artificial Organs, (2008), Vol 15: 3, pp 164-170.

[41] Park JK, Chang HN. Flow Distribution in the Fiber Lumen Side of a Hollow Fiber Module. AIChE J., 32, (1986), pp 1937-1947.

[42] Versteeg HK and Malalasekera W. An introduction to computational fluid dynamics – The finite volume method. Longman Scientific and Technical, 1995.

[43] Frank A, Lipscomb GG, Dennis M. Visualization of Concentration Fields in Hemodialyzers by Computed Tomography, 2000, J. Membr. Sci., 175, pp. 239-251.

[44] Gutknecht J, Bisson MA, Tosteson FC. Effects of Carbon Anhydrase, Bicarbonate and Unstirred Layers. J of General Physiology, 1977, Vol. 69, pp. 779-794.

[45] Lu J and Lu WQ. A Numerical Simulation for Mass Transfer through the Porous Membrane of Parallel Straight Channels. Int. J. of Heat and Mass Transfer 53, (2010) 2404-2413.

[46] Palaty Z and Bendova H. Modeling and Numerical Analysis of Counter-Current Dialyzer at Steady State, Chem. Engr and Processing, 49 (2010) 29-34.

[47] Eloot S, Wachter D, Tricht I, Verdonck P. Computational Flow Modeling in Hollow-Fiber Dialyzer. Artif. Organs (2002) 26(7):590-599.

[48] Tong S and Yuan F. An Equivalent Length Model of Microdialysis Sampling. J. of Pharm. and Biomed. Analysis. 28 (2002) 269-278.

[49] Soudan K, Ricanati ES, Leon JB, Sehgal AR. Determinants of metabolic acidosis among hemodialysis patients. Hemodialysis Int. 2006; 10:209-214.

[50] Ding W, He L, Zhao G et al. Double Porous Media for Mass Transfer of Hemodialyzers. Int.J. of Heat and Mass Transfer 47 (2004) 4849-4855.

[51] Dankwerts PV, Sharma MM. The absorption of carbon dioxide into solutions of alkalis and amines (with some notes on hydrogen sulfide and carbonyl sulfide), Chem. Eng. (October, 1966) 244.

[52] Patzer, J.F., Oxygen consumption in a hollow fiber bioartificial liver-revisited. Artificial Organs, 2004. 28(1): p. 83-98.

[53] Labecki, M., J.M. Piret, and B.D. Bowen, 2-Dimensional Analysis of Fluid-Flow in Hollow-Fiber Modules. Chemical Engineering Science, 1995. 50(21): p. 3369-3384.

[54] Moussy Y. and Snider AD. Laminal Flow over Pipe with Injection and Suction through the Porous Wall at Low Reynolds Number. J. of Membr. Science 327 (2009) 104-107.

[55] Anderson L. Configurational effect on the reflection coefficient for rigid solutes in capillary pores. J. Theor. Bio. 90 (1981) 405-426.

[56] Tong S. and Tuan F. An equivalent length model of microdialysis sampling. J. Phar. & Biomed. Anal. 28 (2002) 269-278.